CrystEngComm

Synthesis and X-Ray Absorption Spectroscopy of Potassium Transition Metal Fluoride Nanocrystals

Journal:	*CrystEngComm*
Manuscript ID	CE-ART-08-2018-001349.R1
Article Type:	Paper
Date Submitted by the Author:	30-Oct-2018
Complete List of Authors:	Plews, Michael; University of Illinois at Chicago, Department of Chemistry Yi, Tanghong; University of Illinois at Chicago, Department of Chemistry Lee, John; E O Lawrence Berkeley National Laboratory Chan, Emory; Lawrence Berkeley National Laboratory, The Molecular Foundry Freeland, John; Argonne National Laboratory Nordlund, Dennis; Stanford Synchrotron Radiation Lightsource, Cabana, Jordi; University of Illinois at Chicago, Department of Chemistry

Journal Name

ARTICLE TYPE

Cite this: DOI: 10.1039/xxxxxxxxxx

Synthesis and X-Ray Absorption Spectroscopy of Potassium Transition Metal Fluoride Nanocrystals†

Michael R. Plews,[a] Tanghong Yi,[a] John Lee,[b] Emory Chan,[b] John W. Freeland,[c] Dennis Nordlund,[d] and Jordi Cabana*[a]

Received Date
Accepted Date

DOI: 10.1039/xxxxxxxxxx

www.rsc.org/journalname

Nanocrystals of KMF$_3$ (M = Mn - Ni) and K$_3M$F$_6$ (M = V, Fe) were synthesized via non-aqueous routes based on colloidal chemistry. The effect of a variety of parameters on the purity, size and quality of the nanocrystals was evaluated. Fluorides formed from mixtures of commercially available potassium trifluoroacetates and transition metal alkoxides, as opposed to existing methods based solely on trifluoroacetate precursors. Particles of KMF$_3$, with a bimodal distribution in the range of several to tens of nanometers, were achieved. It was found that methodologies based on the hot injection precursors often led to crystal sizes an order of magnitude smaller than co-thermolysis as well as higher purity material. X-ray absorption spectroscopy revealed that M-F bond hybridization increased with transition metal d-electron count. Further probing of the Fe K and L edges, making use of different probing depths, KFeF$_3$ nanocrystals were found to have Fe^{II} in the bulk, but the surface was rich in Fe^{III}, but not as the product of oxidation. The developed protocols and lessons learned could be leveraged to rapidly devise synthetic methods for other alkali transition metal fluorides of interest.

1 Introduction

Research into nanosizing materials has grown vastly in the past few decades, the driving force behind it being that interesting new properties of materials begin to present themselves as the size of the material diminishes[1]. In order to understand and enhance these properties, efforts must be made into control of size and shape of these materials. So far, the field has sought to provide standard synthetic conditions and rules for nanocrystal growth resulting in a large library of nanomaterials that exist in a multitude of applications[2–4]. By adding complex phases to this library, understanding of the fundamental self-assembly, crystallization, and growth mechanisms of nanocrystals will continue to evolve.

Complex fluorides with a perovskite structure have interesting electronic, optical and magnetic properties[5,6]. In particular, KMF$_3$ (M = Mn - Fe) have attracted interest in electrochemical applications such as batteries[5], and supercapacitors[7]. In both cases, the use of small particles maximizes surface area, where charge storage is initiated. In the specific case of alkali-ion batteries: (i) fluorides could stabilize higher oxidation states of transition metals by pinning the redox reaction at the metal center. (ii) using a more electronegative anion lowers the Fermi level in the cathode with respect to oxides, thereby raising the operating voltage, and, thus, energy density of the overall cell. In the case of perovskite fluorides, K$^+$ ions have been shown to deintercalate from KFeF$_3$, compensated by oxidation of Fe.[5,8] These results encourage interest in potassium transition metal fluorides, broadly, for electrochemical applications. However, increased ionicity of the M-F bond compared to M-O causes electronic insulation in the material. This issue, reinforces the need for fluoride materials to be formed in the nanoscale to minimize the lengths of electron diffusion. Therefore, synthetic protocols for alkali-transition metal fluorides in nanocrystalline form need to be established. Perovskite-type fluorides have been synthesized previously[9–11], however the authors found no reports of KMF$_3$ (M= Fe, Co) or K$_3M$F$_6$ (M = V, Fe), one report of KNiF$_3$ [7], and several reports of KMnF$_3$ [12–17] whereby these materials were grown colloidally to <100 nm. A common colloidal synthetic protocol relies on the simultaneous decomposition of

---

[a] Department of Chemistry, University of Illinois at Chicago, Chicago, IL, 60607, USA; E-mail: jcabana@uic.edu
[b] The Molecular Foundry, Lawrence Berkeley National Laboratory, Berkeley, CA, 94720, USA
[c] Advanced Photon Source, Argonne National Laboratory, Lemont, IL, 60439, USA
[d] Stanford Linear Accelerator Center, Stanford Synchrotron Radiation Lightsource, Menlo Park, CA, 94025, USA

† Electronic Supplementary Information (ESI) available: Description of synthesis of KFeF$_3$ nanocrystals using iron trifluoroacetate. Full characterization data for materials in this study, including infrared spectroscopy, temperature profile information for KFeF$_3$, results of further parameters used in reactions, and X-ray absorption spectroscopy data providing comparison between standards and samples. See DOI: 10.1039/b000000x/

an alkali trifluoroacetate and a transition metal trifluoroacetate or, alternatively, a bimetallic trifluoroacetate[14], in a solution containing a surfactant in a high boiling point solvent. While this method has proven fruitful, transition metal trifluoroacetates are often unstable or difficult to synthesize. Broadly speaking, defining the need for high concentrations of F in the reaction environment would be valuable.

This study provides synthetic protocols for KMF$_3$ (M = Mn - Ni) and K$_3$$MF_6$ (M = V, Fe) nanocrystals from commercially available precursors, with KMF$_3$ nanocrystals possessing a mean crystal size of <15 nm. We found throughout our study that a transition metal trifluoroacetate was not required, and similar results could be obtained through use of acetates and acetylacetonates, all of which are commercially available.

In addition to synthesis, this study also probes the electronic structure of the resulting nanocrystals using X-ray absorption spectroscopy (XAS), which provides insight into their bonding character by complementary insight at both the transition metal center and the fluoride anion. The resulting materials were characterized by a variety of techniques to confirm the desired chemical composition, structure, and morphology.

2 Experimental

Nickel(II) acetylacetonate, iron(II) acetate, cobalt(II) acetylacetonate, manganese(II) acetate, potassium trifluoroacetate, 1-octadecene, and oleic acid were purchased from Sigma-Aldrich and used without further purification. Oleylamine was purchased from Sigma-Aldrich and was held at 120 °C, degassed, and refilled with nitrogen gas three times over at least a 4 hour period prior to use.

2.1 KMF$_3$ (M = Fe, Co, Ni) and K$_3$$MF_6$ (M = V, Fe) Nanocrystals via Co-Thermolysis

Potassium trifluoroacetate and the metal precursor were weighed in an argon filled glovebox in stoichiometric amounts described in Table 1 and added to a 50 mL three-necked round bottomed flask. The flask was quickly attached to a Schlenk line flowing nitrogen gas. Oleylamine (1.93 g, 6.55 mmol), oleic acid (3.73 g, 13.23 mmol), and 1-octadecene (5.05 g, 20.15 mmol) were stirred vigorously before being added to the flask containing the solids to create a homogeneous solution. The mixture was stirred vigorously, heated to 120 °C at 10 °C min^{-1} and evacuated and refilled with nitrogen three times over a 2 hour period. The solution was subsequently heated to 290 °C at 10 °C min^{-1} (unless described otherwise in Table 1) and held there for 1 hour. Lastly, the solution was allowed to cool naturally to 70 °C. At 70 °C ethanol (20 mL, 200 proof) was added. The precipitated mixture was then centrifuged at 10 000 rpm for 5 min, the supernatant removed, and the solid redispersed in hexane (5 mL). Vortexing and sonication was used to aid redispersion before being reprecipitated with ethanol (10 mL). This procedure was repeated 3-5 times before characterization of the resulting nanocrystals.

2.2 KMF$_3$ (M = Mn, Fe, Co) Nanocrystals via Hot Injection

Potassium trifluoroacetate and the metal precursor were weighed in an argon filled glovebox in stoichiometric amounts described in Table 1 and added to separate 50 mL three-necked round bottomed flasks under a flow of nitrogen. Oleylamine (6.55 mmol, 1.93 g), oleic acid (13.23 mmol, 3.73 g), and 1-octadecene (13.23 mmol, 5.05 g) were stirred vigorously before being split evenly between the two flasks containing the solids. The mixtures were stirred vigorously, heated to 120 °C at 10 °C min^{-1} (unless described otherwise in Table 1), and evacuated and refilled with nitrogen three times over a 2 hour period. The potassium solution was then heated to 290 °C at 10 °C min^{-1}, while the metal solution was kept at its degassing temperature. A cannula was used to pierce and connect the two flasks, and using vacuum, the metal precursor solution was injected into the potassium solution as quickly as possible. The resulting solution settled at 220 °C before being heated at 20 °C min^{-1} to the final reaction temperatures as described in Table 1. The solution was held for 5 min before being allowed to cool naturally to 70 °C. At 70 °C, ethanol (20 mL, 200 proof) was added. The precipitated mixture was then centrifuged at 10 000 rpm for 5 min, the supernatant removed, and the solid redispersed in hexane (5 mL). Vortexing and sonication was used to aid redispersion before being reprecipitated with ethanol (10 mL). This procedure was repeated 3-5 times before characterization of the resulting nanocrystals.

2.3 Characterization

Powder X-ray diffraction (XRD) patterns were obtained in a Bruker D8 Advance diffractometer set up in Bragg-Brentano configuration, using a Cu Kα (λ = 1.5418 Å) source with a step size of 0.02° and a collection time of 1 s per step. The samples were sonicated in hexane before being dropcast on to a Si {111}, zero background wafer and scanned in air. Efforts were made to quantitatively measure representative fractions of the samples and avoid size selection. Transmission electron microscopy (TEM) images were obtained in a JEOL 3010 at 300 keV on glassy carbon coated copper grids (Ted Pella). Size analysis was conducted manually on at least 300 nanocrystals of each material using ImageJ software. All data was collected in accordance to currently accepted methods of nanocrystal size analysis[18,19].

XAS was carried out at selected transition metal *K*- and *L*-edges, as well as the F *K*-edge. Samples for measurements at all *L*-edges and the F *K*-edge (680 eV to 720 eV) prepared by drying powder in a 60 °C vacuum oven, followed by brushing on to carbon tape inside an argon-filled glovebox. Measurements were carried out at beamlines 4-ID-C at the Advanced Photon Source (APS), 8.0.1 at the Advanced Light Source (ALS), and 8-2 at the Stanford Synchrotron Radiation Lightsource (SSRL). At the APS, samples were loaded into the chamber in a glovebag under positive pressure of argon. The measurements were collected at 1×10^{-9} Torr, simultaneously in both the total electron yield (TEY) and total fluorescence yield (TFY) mode, respectively. At the ALS, samples were loaded in a sealed transfer vessel filled with argon. The measurements were performed at 5×10^{-9} Torr.

Data was collected using a current amplifier (Keithley) (TEY) and a Channeltron (TFY) analyzer. At the SSRL, samples were mounted onto an aluminium sample bar using carbon tape inside of a nitrogen glovebox, and transferred without exposure via a nitrogen filled glovebag into the load lock chamber. The measurements were all performed in a single load at 3×10^{-9} Torr, simultaneously collecting TEY (via the sample drain current), TFY (from a silicon diode, AXUV-100), and auger electron yield (AEY) using a double-pass cylindrical mirror analyzer at 200 V pass energy. All spectra were normalized to the incoming flux measured from a gold covered mesh upstream of the main chamber.

Fe K-edge XAS as measured as beamline 20-BM-B at the APS. Samples were prepared by finely grinding the dry powdered material with cellulose (as purchased from Sigma Aldrich) as a binder. The concentrations were calculated to 2.5 x the absorption length of the sample. The mixture was then poured into a hand powered pellet press and compressed to a diameter of 120 mm and thickness of 25 mm. Lastly, the pellet was sealed between two pieces of Kapton tape. Measurements were made in transmission mode using gas ionization chambers to monitor x-ray intensities. A rhodium-coated x-ray mirror was used to reject any higher-order harmonics.

3 Results and Discussion

Recipes of the synthesis of ternary alkali transition metal fluorides available in the literature[20–25] involve the co-thermolysis exclusively of fluorinated organometallic precursors, such as metal trifluoroacetates. A double fluorine source method, whereby both the alkali and transition metal precursors are fluorinated organometallics, proved successful for $KFeF_3$ (see Supporting Information). The necessity of fluorinated transition metal precursor was evaluated in this study to simplify the synthetic procedure[26–29] using commercial sources of first row transition metal precursors. All fluorides could be prepared using $M(CH_3COO)_2$, $M(CH_3COCHCOCH_3)_2$ or $M(CH_3COCHCOCH_3)_3$ instead of $M(CF_3COO)_2$ as previously reported, with $K(CF_3COO)$ as a source of fluorine.

3.1 $KFeF_3$ and K_3FeF_6 Nanocrystals

Due to our familiarity with $KFeF_3$ we aimed to synthesize this material first. $KFeF_3$ and K_3FeF_6 nanocrystals could be synthesized via a co-thermolysis method. Figure 1 revealed the XRD pattern of the nanocrystal products from this method at different temperatures. Indexing of the patterns shows pure K_3FeF_6 (PDF# 00-022-1223) at 200 °C and pure $KFeF_3$ (PDF# 00-020-0895) with some minor K_3FeF_6 at 290 °C, with mixtures of these two phases at intermediate temperatures. Therefore, as the temperature of the reaction was increased, production of Fe^{II} phase over Fe^{III} phase was favoured. This observation implies that K_3FeF_6 is an intermediate in the reactions to produce $KFeF_3$. To test this hypothesis, an aliquot was quenched during co-thermolysis at 290 °C. For comparison purposes, a second final product was prepared after a treatment of co-thermolysis at 290 °C followed by heating at 200 °C for 40 minutes and cooling to room temperature. As expected, the aliquot at 290 °C consisted entirely of $KFeF_3$, which we confirmed by XRD (Figure 1). In turn, $KFeF_3$ was also the majority phase in the final product collected after annealing at 200 °C, with a minor K_3FeF_6 impurity (see Figure S1). The result shows that the final reduction step to form $KFeF_3$ is not reversible. To ensure the purity of the precursor, and to avoid inadvertently starting from a Fe^{III} material, the purity of $Fe(CH_3COO)_2$ was ensured to match the infrared (IR) spectrum (Figure S2) from a previous study[30]. Therefore, the initial oxidation of Fe^{II} to Fe^{III}, before reducing back to Fe^{II}, was unexpected and would require further study.

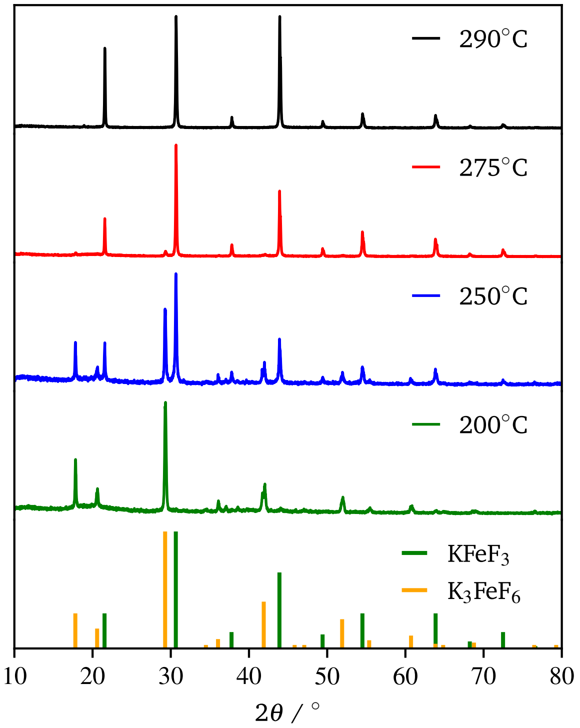

Fig. 1 XRD patterns of the co-thermolysis product at different reaction temperatures. Reference patterns correspond to $KFeF_3$ (PDF# 00-020-0895) and K_3FeF_6 (PDF# 00-022-1223).

Production of $KFeF_3$ and K_3FeF_6 was also independent of the initial stoichiometry of the precursors. Figure 2 shows the resulting XRD patterns of co-thermolysis products, each with different ratios of the precursor materials in the form of very similar product purity of $KFeF_3$, with $\frac{K}{Fe} = 1$, 2, or 3 at 290 °C. In each case, $KFeF_3$ with similar purity was obtained, although $\frac{K}{Fe} = 1.00$ showed some K_3FeF_6. Decreasing the molar ratio of potassium trifluoroacetate to transition metal precursor, there was no noticeable change in yield of KMF_3, but purity decreased with some K_3FeF_6 being present.

While the co-thermolysis of trifluoroacetates of both potassium and iron produced sub-50 nm nanocrystals (Figure S3), the use of transition metal acetates led to larger particles of over 100 nm, both in the case of $KFeF_3$ and K_3FeF_6 (Figures 3a and 4b). All traditional means of crystal size control were evaluated with the goal of a mean size distribution of $<$100 nm. These included

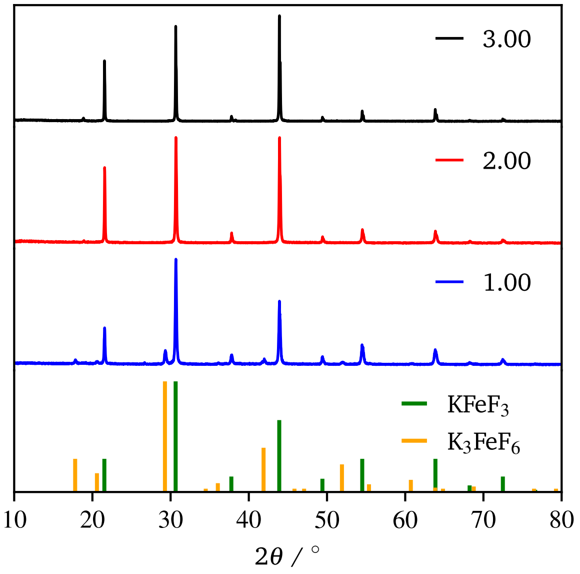

Fig. 2 XRD patterns showing the co-thermolysis product, $KFeF_3$, at different stoichiometries of precursors in the reaction mixture ($\frac{K}{Fe}$). Reference patterns correspond to $KFeF_3$ (PDF# 00-020-0895) and K_3FeF_6 (PDF# 00-022-1223).

(i) choice and concentration of metal precursors[31] (control of growth mechanism and supersaturation), (ii) variation in surfactant composition[4,32–34] (control of growth rate), (iii) reaction temperature[1,21] (control of of nucleation and growth rate). The concentration of the transition metal seemed to have little effect on the size of the resultant nanocrystals (Figure S4). Figure 3 shows XRD patterns corresponding to a variation of the molar ratio between oleylamine (OM) and oleic acid (OA). This change in surfactant ratio did not produce noticeable changes in crystal size after co-thermolysis, as seen by the lack of any obvious broadening in the widths of the XRD peak.

Removal of all oleylamine from the reaction resulted in impurities, while an increase in the molar ratio of oleylamine resulted in a pronounced decrease in intensity of the diffraction reflections corresponding to the <100> crystallographic direction. This observation suggests while size control was not achieved with surfactant composition, some change in relative facet abundance is observed. This conclusion was confirmed in TEM images (Figure 3). While rounded particles were obtained in 100 % oleic acid, the presence of oleylamine led to cubic nanocrystals. Similar control in shape resulting in relative concentration of oleic acid to oleylamine has been demonstrated in fluoride nanocrystals[9,20,21,31,35]. As in that case, it is presumable that the affinity of oleylamine for a certain crystal facet changed the overall shape of the nanocrystal. It is well established to arise from the different surface energies of each crystal facet, causing different affinities for surfactant and precursor attachment at the surface[36].

In efforts to define and control the nucleation period, the iron(II) acetate was injected into a hot flask containing the potas-

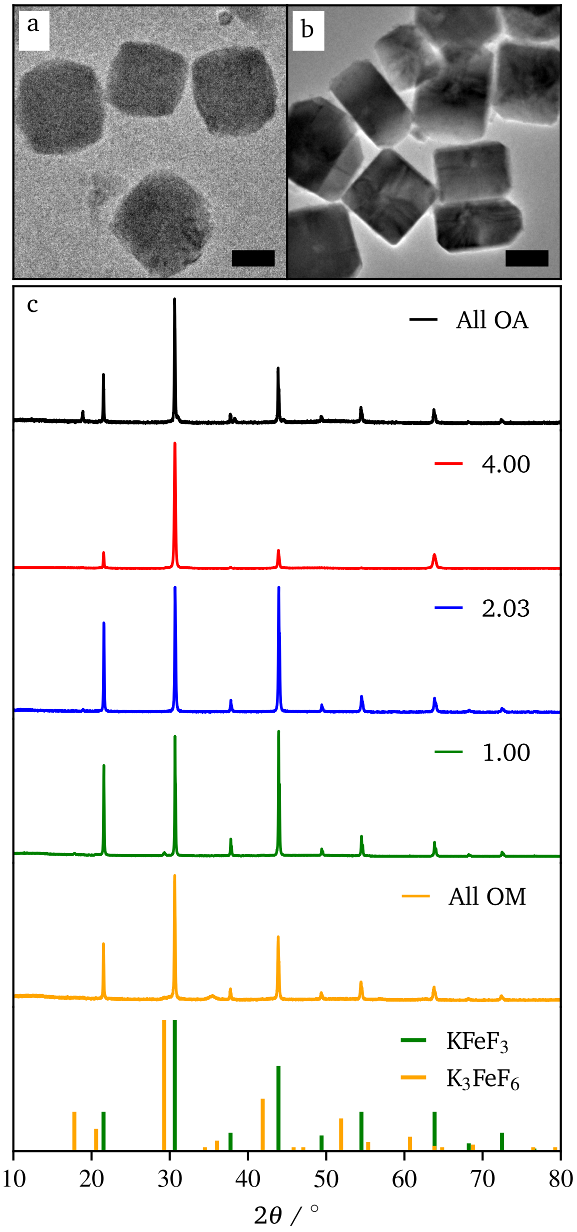

Fig. 3 TEM images of $KFeF_3$ in all oleic acid (a) and surfactant molar ratio $\frac{OA}{OM} = 2.03$ (b) with XRD patterns of co-thermolysis synthesis of $KFeF_3$ while varying the $\frac{OA}{OM}$ molar ratio (c). Reference patterns correspond to $KFeF_3$ (PDF# 00-020-0895) and K_3FeF_6 (PDF# 00-022-1223). Scale bars represent 200 nm.

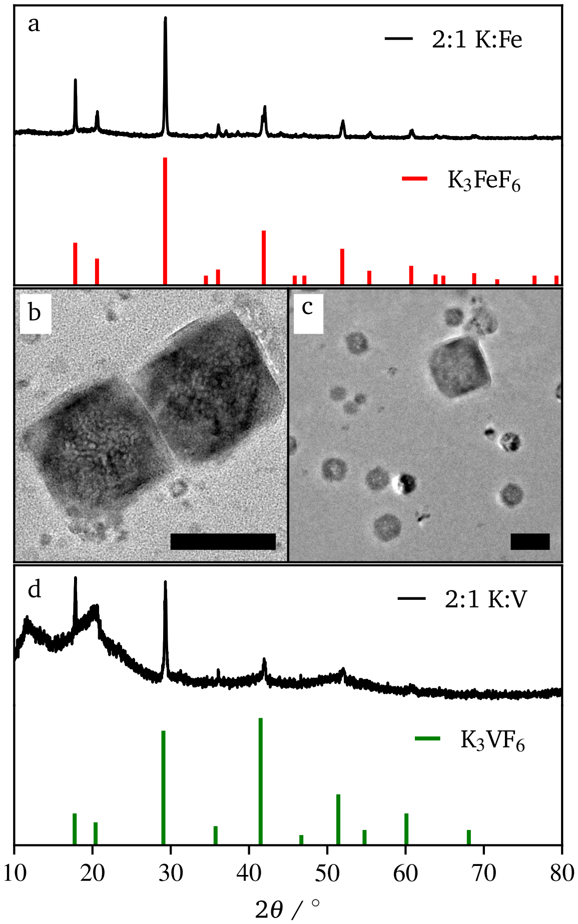

Fig. 4 XRD pattern (a) and TEM image (b) of the co-thermolysis product, K_3FeF_6, as well as TEM image (c) and the XRD pattern (d) of the co-thermolysis product, K_3VF_6. Reference patterns correspond to K_3FeF_6 (PDF# 00-022-1223) and K_3VF_6 (PDF# 00-022-0868). Scale bars represent 100 nm.

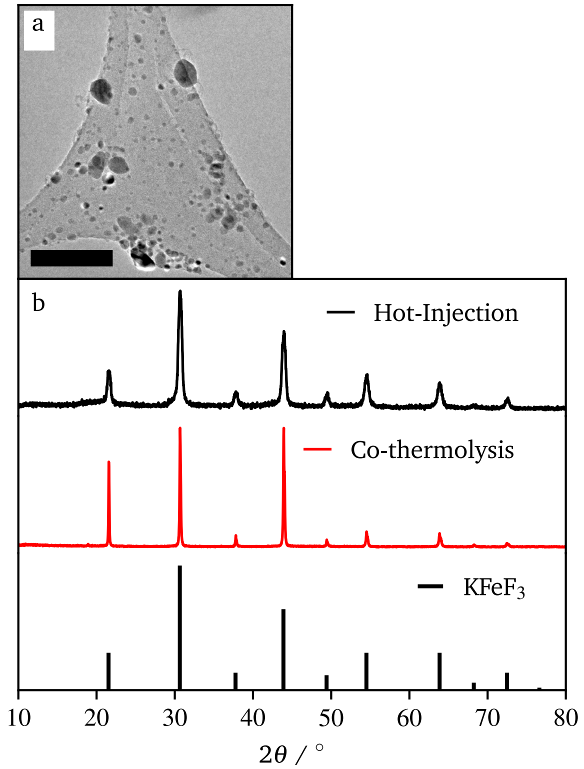

Fig. 5 TEM images of $KFeF_3$ nanoparticles synthesized by hot-injection (a) and XRD patterns representing the same samples (b). The reference pattern corresponds to $KFeF_3$ (PDF# 00-020-0895). Scale bar represents 100 nm.

sium trifluoroacetate. This hot-injection proved to be the most helpful to achieve sub-50 nm crystals. Figure 5 shows the XRD pattern and a representative TEM image of the resulting product. Compared to co-thermolysis (Figure 1), no XRD peaks assigned to K_3FeF_6 were observed, in contrast to samples prepared by co-thermolysis. The product of hot-injection showed substantially wider diffraction peaks than co-thermolysis. However, each peak showed a broad baseline, suggesting overlap of a very small, wide peaks and tall, thin peaks. This effect was due to a bimodal distribution of particle sizes. Indeed, TEM images of the product show that some nanocrystals were very small (∼10 nm), but there was a dispersion in size, with crystals up to 80 nm. Although these distributions were not ideal, the significant difference in size means that the two populations can be separated easily using standard methods such as size selective precipitation.

This approach to the synthesis of $KFeF_3$ shows a reliability of fast nucleation to affect the size of the resulting nanocrystal. Furthermore, the reliability of temperature to define the dominant phase shows that the intermediate, metastable phase of this reaction is K_3FeF_6 while the thermodynamically stable product is $KFeF_3$.

3.2 Nanocrystal Syntheses with Other Transition Metals

In efforts to expand this synthetic model to other first row transition metals, variants with Mn, Ni, and Co were investigated.

$KMnF_3$ could be synthesized via hot-injection (Figure S5). The XRD pattern showed wide peaks, with peak intensities as expected compared to the reference pattern (PDF# 00-017-0116). This shows that the sample underwent no preferred orientation, or preferred facet growth during synthesis. Due to ample examples of $KMnF_3$ nanocrystals in the literature this material was not investigated any further.[12–17] $KNiF_3$ nanocrystals were produced through a simple co-thermolysis (Figure 6 and Table 1). The XRD pattern of the crystals could be indexed with $KNiF_3$ (PDF# 00-021-1002) without the presence of impurities. Figure 6c show TEM images of the $KNiF_3$ nanocrystals synthesized by co-thermolysis at different stoichiometric ratios of precursors, with sizes around 15 nm. As in the case of $KFeF_3$, attempts to synthesize $KCoF_3$ nanocrystals through co-thermolysis of $Co(CH_3COCHCOCH_3)_2$ resulted in particles at sizes around 100 nm. Thin nanoplates of $KCoF_3$ were obtained through the hot-injection method. The products obtained from a reaction at 290 °C (Table 1) were almost transparent (Figure S6a), with Moiré fringes being observed for some overlapping particles. Variations in the $\frac{K}{Co}$ ratio led to subtle changes in the shape and relative intensity of the XRD peaks, which largely matched $KCoF_3$ (PDF# 00-018-1006) with the exception again of an impurity at 18° in $\frac{K}{Co} = 2.00$. The clear difference in relative peak intensities between the samples and the reference pattern is indicative of preferential orientation due to anisotropic crystal growth. Further analysis of Moiré fringes and making use of high-resolution TEM could provide greater insight into the growth directions of the crystal.

In this case, the specific nanocrystal mean size was found to be notably affected by the order in which reagents were injected. Figure S7 compares XRD data for $\frac{K}{Co} = 2.00$ depending on the order of injection of the metal solutions in to the main reaction vessel. When the potassium solution (at 120 °C) was injected to the cobalt solution (at 290 °C), large particles formed. Only when the cobalt solution (at 120 °C) was injected in to the potassium solution (at 290 °C) did sub-50 nm nanocrystals form. The figure shows the drastic difference in Scherrer broadening and therefore, particle size. This effect implies that the rate of nucleation can be increased by decomposing the reagents at different temperatures and combining them to one solution. In the former case, the decomposition of potassium trifluoroacetate in the solvent mixture was not complete at 120 °C, and injecting the precursor to a hot solution of cobalt(II) acetylacetonate resulted in slow decomposition as the temperature ramped thereby limiting the nucleation rate. The latter experiment shows the opposite; the potassium acetate was decomposed at 290 °C and therefore nucleation was not limited immediately after injection.

Synthesis beyond K_3FeF_6 were also attempted. Figures 4c and d shows TEM and XRD data respectively for co-thermolytic

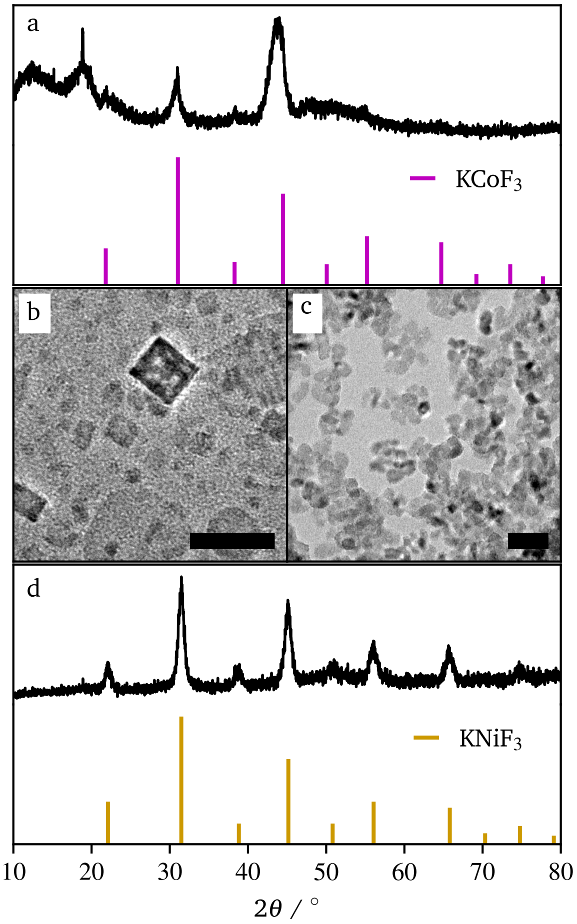

Fig. 6 XRD patterns of $KCoF_3$ (a) and $KNiF_3$ (d) and their respective TEM images (c, d). Reference patterns correspond to $KCoF_3$ (PDF# 00-018-1006) and $KNiF_3$ (PDF# 00-021-1002). Scale bars represent 30 nm.

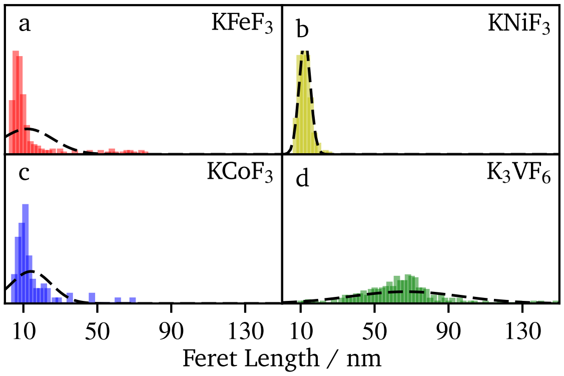

Fig. 7 Histograms depicting TEM size analysis for (a) $KFeF_3$ (b) $KNiF_3$ (c) $KCoF_3$and (d) K_3VF_6. All sample sizes were at least 300 particles. Black dashed lines depict the normal distribution curve for each data set. If the particle was anisotropically shaped, the longest axis was recorded.

synthesis of K_3VF_6. TEM reveals nanocrystals of ∼75 nm, while XRD data showed sharp diffraction peaks representative of this size throughout the entire nanocrystal population. It should be noted that a broad hump at 20° as well as XRD peak intensities not matching the reference pattern (PDF# 00-022-0868) is due to the nature of the collected product; K_3VF_6 could not be collected as a dry powder, and likely still had a lot of organic surfactant on the surface of the particles. It should also be noted that the starting material, $V(CH_3COCHCOCH_3)_3$ is a V^{III} compound, and demonstrates this technique of single fluorine source can be used with both transition metal III and II oxidation states.

A comparative analysis of the size of the nanocrystals prepared by hot-injection ($KFeF_3$ and $KCoF_3$) and co-thermolysis ($KNiF_3$ and K_3VF_6) is presented in Figure 7. The average (mean) sizes of particles and crystallites for all compounds, were collected from TEM and XRD via Scherrer analysis, respectively, and are shown in Table 1. It is worth noting that sizes below 20 nm were obtained in many cases, highlighting the value of the synthetic approach. The results of $KFeF_3$ and $KCoF_3$ reinforce the idea that hot-injection reduced the crystal size by an order of magnitude compared to co-thermolysis, which was only equally effective for $KNiF_3$.

Size distributions were narrow for $KNiF_3$, moderate for $KFeF_3$ and $KCoF_3$, and wide for K_3VF_6. However these particles are not within $\frac{\sigma}{d} < 0.05$ (σ = standard deviation, d = mean), proposed in the literature as a limit to label samples as monodisperse[19]. Further efforts would be needed to further narrow the distribution of these nanocrystals. Only a single normal distribution curve was overlaid to each histogram, but the distribution of $KFeF_3$ by hot-injection may benefit from a bimodal fit, as a large number of outliers exist at 40 nm to 80 nm. Mean particle sizes collected through TEM were of the same order as the crystallite size calculated Scherrer size (Table 1).

To the best of our knowledge, these syntheses result in the lowest mean size of KMF_3 (M = Mn - Ni) and K_3MF_6 (M = V, Fe) currently in the literature.

3.3 Soft X-Ray Absorption Spectroscopy

Probing M-F hybridization effects in these compounds would allow fundamental understanding of redox processes that could be possible with these materials, in view of a potential use as active materials for alkali-ion battery electrodes. To probe chemical bonding, XAS at both the transition metal and fluorine L and K-edges was used. K-edge XAS probes the transitions of core, $1s$ electrons to unoccupied $2p$ states while L-edges arise from the $2p \rightarrow 3d$ dipole allowed transitions.

Figure 8 shows transition metal L-edge spectra for each material synthesized in this work. Each spectrum consists of two regions, the L_3 at lower energy, and the L_2 at higher energy. These regions arise from spin-orbit splitting of the core level $2p_{3/2}$ and $2p_{1/2}$ orbitals respectively. The K_3VF_6 V L-edge (510 eV to 530 eV) splits into the L_3 (510 eV to 520 eV) region and L_2 (520 eV to 530 eV) region. Each of these regions are made up of several overlapping peaks that appear here as shoulders (e.g. 514 eV, 518 eV, 521.5 eV) to the main peaks. The signals in the L_3 region of K_3FeF_6, $KFeF_3$ (705 eV to 712 eV) and $KNiF_3$ (850 eV to 855 eV) each were split into two peaks, while in $KCoF_3$ (775 eV to 783 eV) it was split finely into multiple peaks. The L_2 region for K_3FeF_6, $KFeF_3$ (720 eV to 725 eV) and $KNiF_3$ (868 eV to 872 eV) further splits to two peaks, while this region in $KCoF_3$ (792 eV to 795 eV) showed a rather broad feature with a shoulder at high energy. Comparison of $KCoF_3$ (Figure 8c) with literature data for CoF_2 [37] revealed similarities in the fine splitting of multiplet peaks, confirming the presence of Co^{II} in the ternary fluoride. It should be noted however that the multiplet peaks of L_3 in $KCoF_3$ have slightly different peak intensities when compared with CoF_2. Likewise, the Ni L-edge spectrum of $KNiF_3$ (Figure 8d) presented multiplets in L_3 and L_2 characteristic of Ni^{II} compounds, such as NiF_2 and NiO [38,39] which are due to coulomb and exchange interactions between the core hole and the $3d$ shell. The peak location and shape in the V L-edge spectrum of K_3VF_6 compared well to other V^{III} compounds found in the literature[40]. The peak seen at 529 eV can be attributed to oxygen signal from impurities in the sample due to the surfactants and colloidal methods used to prepare the nanocrystals, as well as the carbon support used to mount the powders. These comparisons confirm the oxidation state of our samples are all as expected when compared to literature samples of their binary counterparts.

The K_3FeF_6 and $KFeF_3$ Fe L-edge spectra (Figure 8b) appear similar in peak shape and energy when compared to literature examples of FeF_3 and FeF_2,[41] as well as our own previous studies on $KFeF_3$ [5]. The peak splitting in the L_3 region appears as peaks at 707.3 eV and 709.1 eV. The high intensity of the peak feature in K_3FeF_6 (Figure 8b) is consistent with the presence of Fe^{III} in the sample. The opposite is characteristic of Fe^{II} compounds. However the TEY spectrum of $KFeF_3$ nanocrystals synthesized in this study (Figure 8b) showed almost equal intensity between the peak at 707.3 eV and the peak at 709.1 eV, suggesting a mixed Fe^{II}/Fe^{III} state.

Material	Precursor (+K(CF_3COO))	Method	K:*M* / mmol	TEM Size / nm	Scherrer Analysis / nm
$KMnF_3$	Mn(CH_3COO)$_2$	Hot-injection	4:2	~15	
$KFeF_3$	Fe(CH_3COO)$_2$	Co-thermolysis	2:1	~350	
		Hot-injection[a]	4:2	12.1±13.8	30
K_3FeF_6	Fe(CH_3COO)$_2$	Co-thermolysis[b]	2:1	~150	
$KCoF_3$	Co($CH_3COCHCOCH_3$)$_2$	Co-thermolysis	2:1	~100	
		Hot-injection	2:1	14.2±10.9	31
$KNiF_3$	Ni($CH_3COCHCOCH_3$)$_2$	Co-thermolysis	3:1	12.2±3.1	12
K_3VF_6	V($CH_3COCHCOCH_3$)$_3$	Co-thermolysis	2:1	67.0±29.8	38

[a] Degassed at 60 °C
[b] Final reaction temperature 200 °C

Table 1 Synthetic summary from this work. Sizes are either reported as approximations for larger particles, or as $d \pm \sigma$ (d = mean, σ = standard deviation) for nanoparticles.

The Fe *L*-edge XAS data can be affected by surface impurities because signal detection occurred through the generation of photoelectrons, that have shallow escape lengths. Therefore, data was also collected at the Fe *K*-edge for $KFeF_3$, and as-purchased FeF_3 and FeF_2 samples (Figure 9a). The high energy X-rays (over 7000 eV) allow measurements in transmission where the bulk state of the sample dominates the signal. As expected, the Fe *K*-edge spectrum of $KFeF_3$ presented a whiteline with an edge jump at a similar energy as FeF_2, and 6 eV lower than FeF_3. It confirmed that the bulk of the ternary fluoride was Fe^{II}. Further evidence of gradients in oxidation state with probing depth resulted from comparing the Fe *L*-edge spectra of $KFeF_3$ collected in AEY (1 nm probing depth), TEY (~1 nm to 3 nm probing depth) and TFY (>10 nm probing depth) modes (Figure 9b). The spectra gained intensity at 707.3 eV, at the expense of 709.1 eV, as the probing depth increased. The spectrum shows the $KFeF_3$ edge closer to that of FeF_2 than FeF_3. Overall, the results lead to the conclusion that the $KFeF_3$ sample contains a majority of Fe^{II}, with a surface layer of Fe^{III}. To rule out the possibility of the formation of Fe_2O_3 on the surface, and in addition to manipulating the sample in conditions as rigorously free of air as possible, O *K*-edge data was also recorded (Figure S8). The spectrum is very close to reference data for the carbon tape substrate. In contrast, the spectrum presented notable differences compared to literature data for Fe_2O_3[42]. These data rule out a significant contribution of surface oxidation, instead suggesting that Fe^{III} remained on the surface of the $KFeF_3$ nanocrystals. The origin of these electronic defects at the surface of the crystals is unclear. It is worth noting that defective $K_{1\text{-}x}FeF_3$ structures have been reported to exist in the literature[43]. These deficient compositions would show Fe^{III}; it is possible that they are favoured on the surface of the nanocrystals.

Figure 10 shows F *K*-edge data for K_3VF_6, K_3FeF_6, $KFeF_3$, $KNiF_3$, and $KCoF_3$. These spectra again compared well in the edge energy and overall peak shape with data for the corresponding binary fluorides (VF_3, FeF_3, FeF_2, CoF_2, and NiF_2) found in the literature[44,45]. The spectra showed a similar peak shape throughout the series. The position of the absorption edge, at 690 eV was maintained throughout the series. The post edge region (690 eV to 720 eV), associated with transitions involving metal 4*sp*-F 2*s* states[44] was similar, with some minor differences throughout the

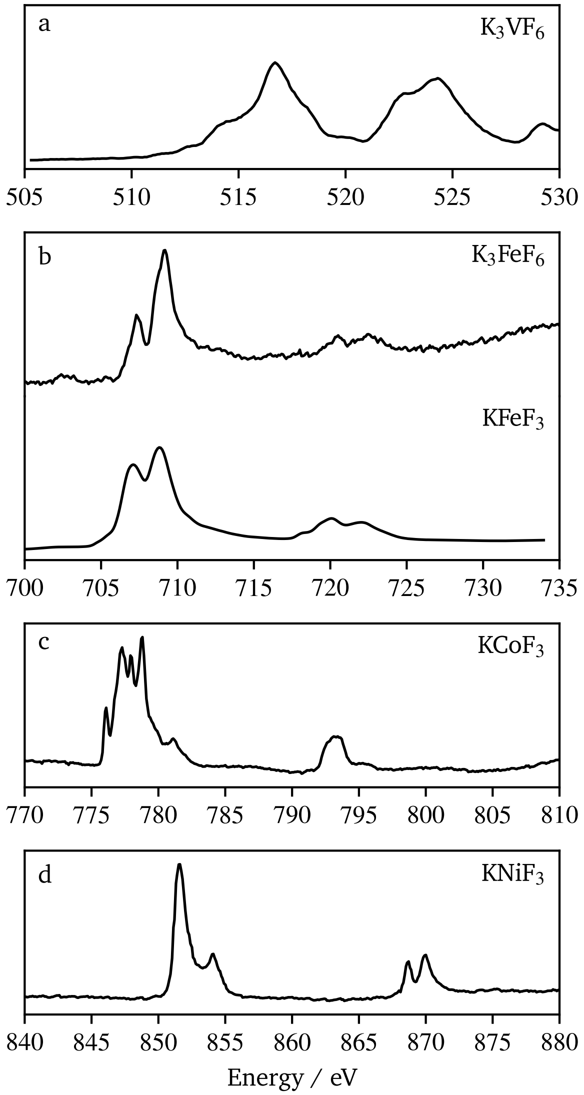

Fig. 8 Transition metal *L*-edge XAS spectra of (a) K_3VF_6, (b) K_3FeF_6 and $KFeF_3$, (c) $KCoF_3$, and (d) $KNiF_3$. Spectra (b-d) are collected in TEY mode, however due to low signal, (a) is collected in TFY mode.

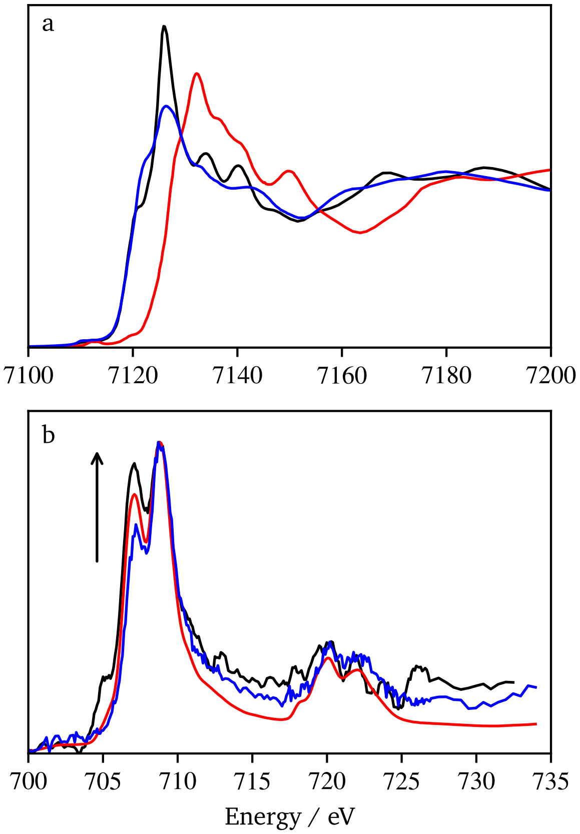

Fig. 9 (a) Hard XAS data comparing X-ray absorption near-edge spectroscopy (XANES) spectra of $KFeF_3$ (black), FeF_3 (red), FeF_2 (blue), and (b) soft XAS data showing TFY (black), TEY (red), and AEY (blue) signals. The arrow depicts the rising intensity of the peak at 707.3 eV as sample penetration increases.

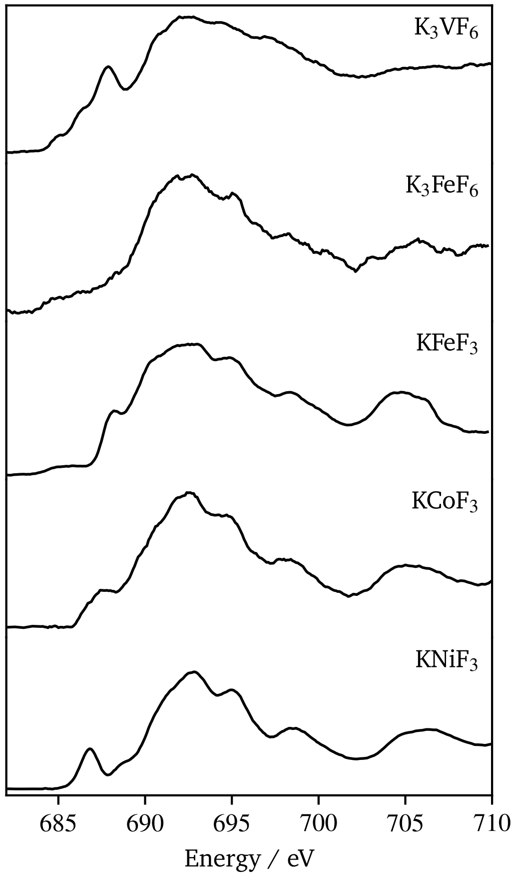

Fig. 10 Fluorine *K*-edge XAS (total fluorescence yield) spectra of K_3VF_6, K_3FeF_6, $KFeF_3$, $KCoF_3$, and $KNiF_3$ nanoparticles.

series. The most pronounced differences were observed in the pre-edge region (680 eV to 690 eV), which corresponds to transitions associated with metal $3d$-F $2p$ hybridized states, and tends to increase in intensity with covalence[46]. In the case of KMF_3, the pre-edge peak was found to emerge and shift to lower energy with increasing atomic number. The pre-edge features in the F data of $KCoF_3$ and, especially, $KNiF_3$ suggests the existence of hybridization between cations and anions. The observed covalence shrinks the band gap, which explains the resulting powder colors from the synthesized nanocrystals (Figure S9). A clear pre-edge with complex line shape was also observed for K_3VF_6, whereas washed out signals were found in K_3FeF_6. The trends in pre-edge intensity with specific transition metal mirrored those reported for binary fluorides[42]. Nonetheless, it should be noted that the M^{II} ternary fluorides possess much more defined peaks at energies greater than 690 eV when compared to NiF_2, CoF_2,[44] and FeF_2[45] (Figure S10). A possible explanation for this could be increased long range order in the perovskite structure. These changes are not reflected in the K_3MF_6 materials.

4 Conclusion

This work reports the synthesis of nanocrystals of KMF$_3$ (M = Mn - Ni) and K$_3M$F$_6$ (M = V) whereby only one reagent was fluorinated. K_3FeF_6 was isolated as an intermediate product in the synthesis of $KFeF_3$. In the case of $KCoF_3$ and $KFeF_3$, the particle shape and facet growth was found to change with the surfactant ratio and relative precursor stoichiometry, producing very thin nanoplates in some extremes. The greatest control over the size and dispersion of the perovskite nanocrystals was achieved using hot injections to quickly introduce and decompose the reagents simultaneously. The formal redox states of the metals were found to be consistent with the stoichiometry of the materials in the bulk of the nanocrystal. Combining bulk signal from Fe K-edge, and varying the probing depths of signal from Fe L-edge spectroscopy, we have shown that synthesis of $KFeF_3$ through hot-injection possessed residual Fe^{III} on the surface of the nanocrystal. The surface species is not as a result of oxidation and would require further study. Production of highly crystalline nanometric fluorides using the generalizable recipes developed in this study will enable their investigation as materials for a variety of applications.

5 Acknowledgements

Support for this research was provided by research start-up funding by the Department of Chemistry and the College of Liberal Arts and Sciences at the University of Illinois at Chicago. Initial synthetic design work at the Molecular Foundry was supported by the Office of Science, Office of Basic Energy Sciences, of the U.S. Department of Energy under Contract No. DE-AC02-05CH11231. This research used resources of the Advanced Light Source, which is a DOE Office of Science User Facility under contract no. DE-AC02-05CH11231. Use of the Advanced Photon Source was supported by the U. S. Department of Energy, Office of Science, Office of Basic Energy Sciences, under Contract No. DE-AC02-06CH11357. Use of the Stanford Synchrotron Radiation Lightsource, SLAC National Accelerator Laboratory, is supported by the U.S. Department of Energy, Office of Science, Office of Basic Energy Sciences under Contract No. DE-AC02-76SF00515. The authors specifically thank Drs. Jingua Guo and Yi-Sheng Liu of the Advanced Light Source, and Dr. Mahalingam Balasubramanian of the Advanced Photon Source for help in preforming XAS measurements.

Conflicts of Interest

There are no conflicts to declare.

References

1 J. Park, J. Joo, S. G. Kwon, Y. Jang and T. Hyeon, *Angew. Chem. Int. Ed. Engl.*, 2007, **46**, 4630–60.

2 C. de Mello Donegá, P. Liljeroth and D. Vanmaekelbergh, *Small*, 2005, **1**, 1152–62.

3 A. S. Aricò, P. Bruce, B. Scrosati, J.-M. Tarascon and W. van Schalkwijk, *Nat. Mater.*, 2005, **4**, 366–377.

4 G. Shao, G. Chen, W. Yang, T. Ding, J. Zuo and Q. Yang, *Langmuir*, 2014, **30**, 2863–2872.

5 T. Yi, W. Chen, L. Cheng, R. D. Bayliss, F. Lin, M. R. Plews, D. Nordlund, M. M. Doeff, K. A. Persson and J. Cabana, *Chem. Mater.*, 2017, **29**, 1561–1568.

6 A. C. Garcia-Castro, A. H. Romero and E. Bousquet, *Phys. Rev. Lett.*, 2016, **116**, 117202.

7 R. Ding, X. Li, W. Shi, Q. Xu, X. Han, Y. Zhou, W. Hong and E. Liu, *J. Mater. Chem. A*, 2017, **5**, 17822–17827.

8 D. Cao, C. Yin, D. Shi, Z. Fu, J. Zhang and C. Li, *Adv. Funct. Mater.*, 2017, **27**, 1701130.

9 H.-X. Mai, Y.-W. Zhang, R. Si, Z.-G. Yan, L.-d. Sun, L.-P. You and C.-H. Yan, *J. Am. Chem. Soc.*, 2006, **128**, 6426–36.

10 H.-X. Mai, Y.-W. Zhang, L.-D. Sun and C.-H. Yan, *J. Phys. Chem. C*, 2007, **111**, 13730–13739.

11 E.-H. Song, S. Ding, M. Wu, S. Ye, F. Xiao, G.-P. Dong and Q.-Y. Zhang, *J. Mater. Chem. C*, 2013, **1**, 4209.

12 J. Wang, F. Wang, C. Wang, Z. Liu and X. Liu, *Angew. Chem. Int. Ed. Engl.*, 2011, **50**, 10369–72.

13 Z. Huang, M. Yi, H. Gao, Z. Zhang and Y. Mao, *J. Alloys Compd.*, 2017, **694**, 241–245.

14 B. D. Dhanapala, H. N. Munasinghe, L. Suescun and F. A. Rabuffetti, *Inorg. Chem.*, 2017, **56**, 13311–13320.

15 L. N. Hao, K. Liu, S. Cheng, Y. Wang, Y. J. Xu and H. S. Qian, *Mater. Lett.*, 2017, **196**, 145–148.

16 Y. Zhang, F. Wang, Y. Lang, J. Yin, M. Zhang, X. Liu, D. Zhang, D. Zhao, G. Qin and W. Qin, *J. Mater. Chem. C*, 2015, **3**, 9827–9832.

17 L. Lei, J. Zhou, J. Zhang and S. Xu, *CrystEngComm*, 2015, **17**, 8457–8462.

18 M. Baalousha and J. R. Lead, *Nat. Nanotechnol.*, 2013, **8**, 308–309.

19 C. J. Murphy and J. M. Buriak, *Chem. Mater.*, 2015, **27**, 4911–4913.

20 Y.-P. Du, Y.-W. Zhang, L.-D. Sun and C.-H. Yan, *Dalton Trans.*, 2009, 8574–81.

21 Y.-P. Du, Y.-W. Zhang, Z.-G. Yan, L.-D. Sun, S. Gao and C.-H. Yan, *Chem. Asian J.*, 2007, **2**, 965–74.

22 J. Boyer, L. Cuccia and J. Capobianco, *Nano Lett.*, 2007, **7**, 847–852.

23 F. Vetrone, R. Naccache, V. Mahalingam, C. G. Morgan and J. A. Capobianco, *Adv. Funct. Mater.*, 2009, **19**, 2924–2929.

24 V. Mahalingam, F. Vetrone, R. Naccache, A. Speghini and J. A. Capobianco, *J. Mater. Chem.*, 2009, **19**, 3149–3152.

25 E. M. Chan, G. Han, J. D. Goldberg, D. J. Gargas, A. D. Ostrowski, P. J. Schuck, B. E. Cohen and D. J. Milliron, *Nano Lett.*, 2012, **12**, 3839–45.

26 M. Puri, R. D. Sharma and R. C. Verma, *Synth. React. Inorg. Met. Chem.*, 1981, **11**, 539–546.

27 F. Calderazzo, U. Englert, G. Pampaloni, V. Passarelli, G. Serni and R. Wang, *Can. J. Chem.*, 2001, **79**, 495–501.

28 N. Iranpoor and H. Adibi, *Bull. Chem. Soc. Jpn.*, 2000, **73**, 675–680.

29 F. Marchetti, F. Marchetti, B. Melai, G. Pampaloni and S. Zacchini, *Inorg. Chem.*, 2007, **46**, 3378–3384.

30 H. G. M. Edwards and I. R. Lewis, *J. Mol. Struct.*, 1993, **296**, 15–20.

31 X. Sun, Y.-W. Zhang, Y.-P. Du, Z.-G. Yan, R. Si, L.-P. You and C.-H. Yan, *Chemistry*, 2007, **13**, 2320–32.

32 Y. Yamada, T. Doi, I. Tanaka, S. Okada and J.-i. Yamaki, *J. Power Sources*, 2011, **196**, 4837–4841.

33 E. M. Chan, C. Xu, A. W. Mao, G. Han, J. S. Owen, B. E. Cohen and D. J. Milliron, *Nano Lett.*, 2010, **10**, 1874–85.

34 N. R. Jana, Y. Chen and X. Peng, *Chem. Mater.*, 2004, **16**, 3931–3935.

35 Y. Lu, Z.-Y. Wen, J. Jin, X.-W. Wu and K. Rui, *Chem. Commun. (Camb).*, 2014, **50**, 6487–90.

36 Y.-w. Jun, M. F. Casula, J.-H. Sim, S. Y. Kim, J. Cheon and A. P. Alivisatos, *J. Am. Chem. Soc.*, 2003, **125**, 15981–15985.

37 D. K. Bora, X. Cheng, M. Kapilashrami, P. A. Glans, Y. Luo and J.-H. Guo, *J. Synchrotron Radiat.*, 2015, **22**, 1450–1458.

38 H. Wang, P. Ge, C. G. Riordan, S. Brooker, C. G. Woomer, T. Collins, C. a. Melendres, O. Graudejus, N. Bartlett and S. P. Cramer, *J. Phys. Chem. B*, 1998, **102**, 8343–8346.

39 H. Wang, S. M. Butorin, A. T. Young and J. Guo, *J. Phys. Chem. C*, 2013, **117**, 24767–24772.

40 D. Maganas, M. Roemelt, T. Weyhermüller, R. Blume, M. Hävecker, A. Knop-Gericke, S. DeBeer, R. Schlögl and F. Neese, *Phys. Chem. Chem. Phys.*, 2014, **16**, 264–276.

41 M. S. M. Saifullah, G. a. Botton, C. B. Boothroyd and C. J. Humphreys, *J. Appl. Phys.*, 1999, **86**, 2499–2504.

42 F. M. F. de Groot, M. Grioni, J. C. Fuggle, J. Ghijsen, G. A. Sawatzky and H. Petersen, *Phys. Rev. B*, 1989, **40**, 5715–5723.

43 S. A. Reisinger, M. Leblanc, A.-M. Mercier, C. C. Tang, J. E. Parker, F. D. Morrison and P. Lightfoot, *Chem. Mater.*, 2011, **23**, 5440–5445.

44 A. S. Vinogradov, S. I. Fedoseenko, S. A. Krasnikov, A. B. Preobrajenski, V. N. Sivkov, D. V. Vyalikh, S. L. Molodtsov, V. K. Adamchuk, C. Laubschat and G. Kaindl, *Phys. Rev. B*, 2005, **71**, 045127.

45 W. Yang, X. Liu, R. Qiao, P. Olalde-Velasco, J. D. Spear, L. Roseguo, J. X. Pepper, Y. D. Chuang, J. D. Denlinger and Z. Hussain, *J. Electron Spectros. Relat. Phenomena*, 2013, **190**, 64–74.

46 J. Suntivich, W. T. Hong, Y.-L. Lee, J. M. Rondinelli, W. Yang, J. B. Goodenough, B. Dabrowski, J. W. Freeland and Y. Shao-Horn, *J. Phys. Chem. C*, 2014, **118**, 1856–1863.